

Enrichment by extragalactic first stars in the Large Magellanic Cloud

Received: 17 December 2023

Accepted: 30 January 2024

Published online: 20 March 2024

 Check for updates

Anirudh Chiti  ^{1,2}, Mohammad Mardini ^{3,4,5,6}, Guilherme Limberg  ^{1,2,7}, Anna Frebel  ^{5,6}, Alexander P. Ji  ^{1,2}, Henrique Reggiani  ⁸, Peter Ferguson  ⁹, Hillary Diane Andales  ^{5,6}, Kaley Brauer ^{5,10}, Ting S. Li  ^{11,12} & Joshua D. Simon  ¹³

The Large Magellanic Cloud (LMC) is the Milky Way's most massive satellite galaxy, which only recently (~2 billion years ago) fell into our Galaxy. As stellar atmospheres preserve the composition of their natal cloud, the LMC's recent infall makes its most ancient, metal-deficient ('low-metallicity') stars unique windows into early star formation and nucleosynthesis in a formerly distant region of the high-redshift universe. Here we present the elemental abundances of ten stars in the LMC with iron-to-hydrogen ratios ranging from ~1/300th to ~1/12,000th that of the Sun. Our most metal-deficient star is markedly more metal-deficient than any in the LMC with available detailed chemical abundance patterns and was probably enriched by a single extragalactic 'first-star' supernova. This star lacks appreciable carbon enhancement, as does our overall sample, unlike the lowest-metallicity stars in the Milky Way. This and other abundance differences affirm that the extragalactic early LMC experienced diverging enrichment processes compared to the early Milky Way. Early element production, driven by the earliest stars, thus, appears to proceed in an environment-dependent manner.

The Large Magellanic Cloud (LMC) is unique among the Milky Way's satellite galaxies in being nearly a major galaxy in its own right (dark matter mass $1.9 \times 10^{11} M_{\odot}$; refs. [1,2](#)) and is thought to have very recently fallen into the Milky Way^{[3,4](#)}. Consequently, the LMC's lowest-metallicity stars provide a unique comparison to those in our Galaxy. Such stars preserve the elemental signatures of early supernovae^{[5–7](#)} in another proto-galactic environment. Moreover, the LMC's recent infall implies that its low-metallicity stars may enable tests of whether the earliest element enrichment and star formation in distant, extragalactic proto-galaxies deviated from what occurred in the proto-Milky Way.

We performed a search for low-metallicity stars in the LMC by applying metallicity-sensitive photometric selections to data from Data Release 3 (DR3) of the Gaia mission^{[8](#)}. We selected probable LMC member stars by identifying all stars within 10° of its centre that had Gaia DR3 proper motions consistent with its bulk motion^{[9,10](#)}. We then derived metallicities for these stars by calculating their simulated flux in metallicity-sensitive passbands^{[11,12](#)} using spectrophotometric data from Gaia Blue and Red Photometer (that is, BP/RP, XP) spectra^{[13](#)}. These fluxes were compared to fluxes from synthetic stellar spectra at various metallicities^{[14](#)} (Methods) to select stars with metallicities below that of the most metal-poor red giant star in the LMC with detailed chemical

¹Department of Astronomy & Astrophysics, University of Chicago, Chicago, IL, USA. ²Kavli Institute for Cosmological Physics, University of Chicago, Chicago, IL, USA. ³Department of Physics, Zarqa University, Zarqa, Jordan. ⁴Jordanian Astronomical Virtual Observatory, Zarqa University, Zarqa, Jordan.

⁵Joint Institute for Nuclear Astrophysics—Center for the Evolution of the Elements (JINA-CEE), East Lansing, MI, USA. ⁶Department of Physics and Kavli Institute for Astrophysics and Space Research, Massachusetts Institute of Technology, Cambridge, MA, USA. ⁷Universidade de São Paulo, Instituto de Astronomia, Geofísica e Ciências Atmosféricas, Departamento de Astronomia, São Paulo, Brazil. ⁸Gemini Observatory/NFS's NOIRLab, La Serena, Chile.

⁹Department of Physics, University of Wisconsin–Madison, Madison, WI, USA. ¹⁰Harvard–Smithsonian Center for Astrophysics, Cambridge, MA, USA.

¹¹Department of Astronomy and Astrophysics, University of Toronto, Toronto, Ontario, Canada. ¹²Dunlap Institute for Astronomy & Astrophysics, University of Toronto, Toronto, Ontario, Canada. ¹³The Observatories of the Carnegie Institution for Science, Pasadena, CA, USA.  e-mail: achiti@uchicago.edu

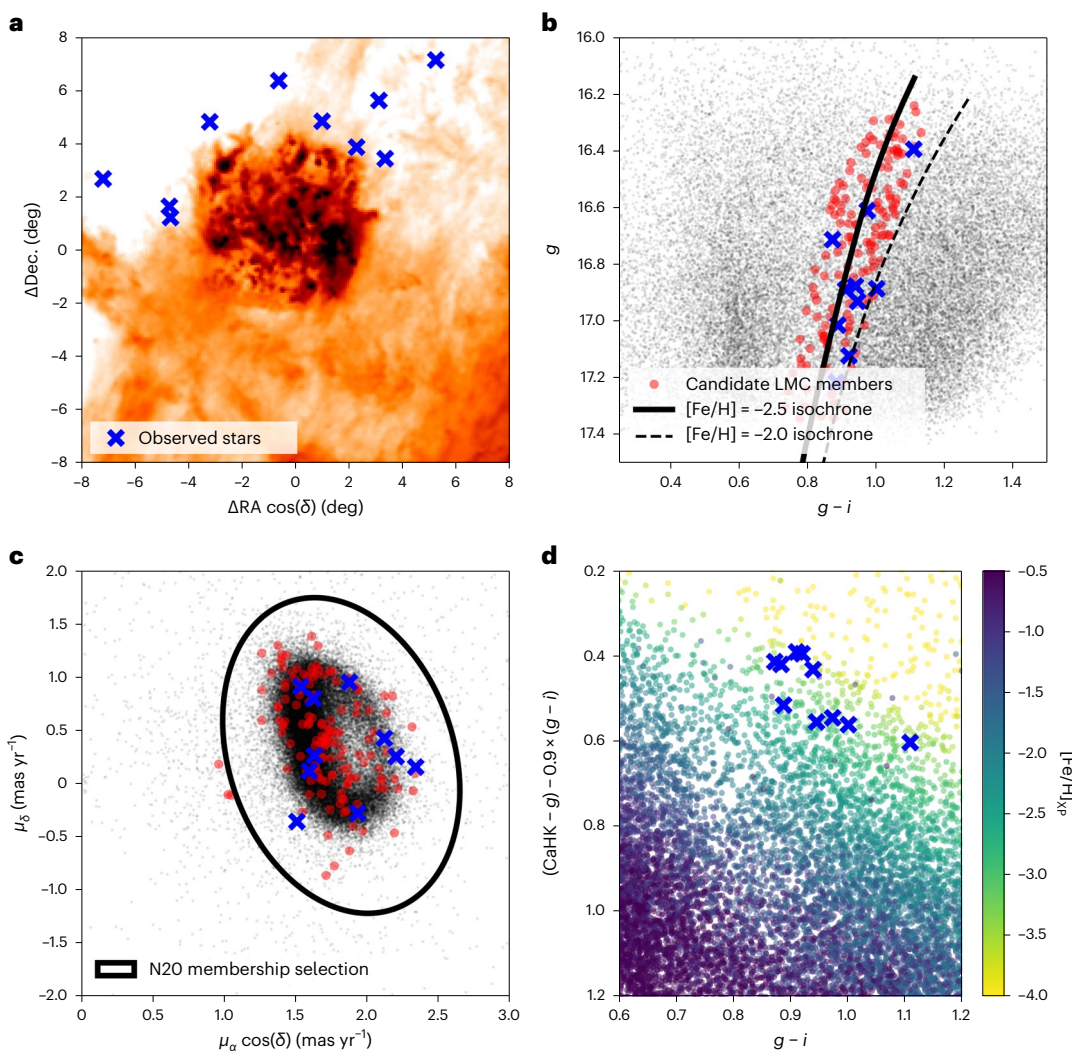


Fig. 1 | Identification of low-metallicity member stars in the LMC. **a**, Locations of low-metallicity LMC member stars observed in this study are indicated by blue crosses. Coordinates are centred on the LMC (right ascension (RA) 5 h 23 min 34 s, declination (dec.) $-69^{\circ} 45' 22''$). The colours in the background indicate reddening $E(B-V)$ values from a canonical dust map⁵⁴. We avoided regions of high reddening in our target selection, as these regions suppress the signal in the blue region of the Gaia XP spectra. **b**, A colour–magnitude diagram of stars within 10° of the LMC, with tracks (isochrones) corresponding to a 12 Gyr, $[Fe/H] = -2.5$ stellar population (solid black line) and 12 Gyr, $[Fe/H] = -2.0$ stellar population (dashed black line)⁵⁵. Stars with LMC-consistent proper motions and locations consistent with the $[Fe/H] = -2.5$ isochrone are shown in red. Our observed stars are, again, shown as blue crosses. Other stars are shown as grey points. **c**, Proper motions of stars within 10° of the LMC centre, where $\mu_{\alpha} \cos(\delta)$

and μ_{δ} correspond to the proper motion in the RA and dec. directions, respectively. The boundary of the membership selection in ref. 9 denoted as a black ellipse labeled N20. Stars passing a proper motion and isochrone selection are shown in red, observed stars are blue crosses and other stars are shown in grey. **d**, Metallicity-sensitive colour–colour plot of all stars within 10° of the LMC, generated from synthetic photometry from the Gaia XP spectra using XPYtools^{8,13}. Each data point is coloured by the metallicity as inferred from this colour–colour plot using methods in ref. 14. Note that all stars that were observed, as indicated by the blue crosses, occupy the low-metallicity space in this colour–colour plot. For clarity, also note that avoiding stars that, for example, have large flux uncertainties, are faint or have nearby companions shaped our choice of candidates to observe from the low-metallicity candidates.

abundances at the time ($[Fe/H] = -2.4$ (ref. 15), where $[Fe/H]$ is defined as the logarithmic iron-to-hydrogen ratio relative to the Sun), although stars down to $[Fe/H] = -3.15$ have very recently been characterized^{16,17}. Figure 1 outlines this selection procedure, starting with the spatial distribution of these stars (Fig. 1a), a colour–magnitude diagram of the LMC field (Fig. 1b), the proper motions of these stars (Fig. 1c) and a colour–colour plot to flag low-metallicity candidates (Fig. 1d).

We obtained follow-up spectra of these candidates using the high-resolution Magellan Inamori Kyocera Echelle (MIKE) spectrograph¹⁸ on the 6.5 m Magellan-Clay telescope. We identified ten stars with metallicities of $-4.2 < [Fe/H] < -2.5$ (see Table 1 and Extended Data Table 1 for a summary of observations), the lowest metallicity of which is an order of magnitude more metal-poor than any previously

detected^{16,17}. We derived abundances for up to 23 elements for our sample using standard one-dimensional stellar model atmospheres under the assumption of local thermodynamic equilibrium¹⁹. The radial velocities measured from these spectra confirm that these stars are gravitationally bound members of the LMC, shown by integrating their orbits in a gravitational potential model that included both the LMC and the Milky Way²⁰ (Methods).

Star LMC 119 has the lowest metallicity in our sample ($[Fe/H] = -4.15 \pm 0.20$) and is the lowest-metallicity star known in any external galaxy²¹. Given its extremely low metallicity, this star exhibits the characteristics of a second-generation star that preserves the chemical imprints of a first-star supernova^{6,7}. Highlighting its uniqueness, the LMC’s earliest stars probably formed when it was at a comoving

Table 1 | Stars in the LMC observed with the high-resolution Magellan/MIKE spectrograph for detailed element abundance analysis in this work

Name	Right ascension	Declination	<i>g</i>	<i>T_{eff}</i> (K)	log(g)	<i>v_{mic}</i> (km s ⁻¹)	[Fe/H]
LMC 003	04:53:37.090	-64:43:57.55	17.05	4,540±158	0.80±0.33	2.90±0.28	-2.97±0.20
LMC 100	04:33:47.361	-67:37:31.51	17.36	4,612±162	1.10±0.32	2.63±0.29	-2.67±0.22
LMC 104	05:18:01.352	-63:22:26.56	16.50	4,531±155	1.05±0.31	2.89±0.28	-2.56±0.21
LMC 109	04:12:01.964	-66:00:58.36	17.01	4,504±155	1.10±0.31	2.58±0.28	-2.85±0.20
LMC 119	05:51:51.026	-63:56:37.60	16.85	4,315±207	0.80±0.33	2.66±0.28	-4.15±0.20
LMC 124	06:08:14.982	-62:07:23.33	16.76	4,531±160	1.10±0.32	2.78±0.29	-2.97±0.21
LMC 204	04:33:20.143	-68:02:41.87	17.30	4,594±173	0.95±0.36	3.02±0.34	-2.83±0.27
LMC 206	05:45:46.652	-65:46:35.40	17.08	4,720±170	1.65±0.34	2.56±0.31	-2.56±0.24
LMC 207	05:32:54.917	-64:53:09.88	17.10	4,486±172	0.80±0.30	2.57±0.32	-3.34±0.25
LMC 215	05:56:37.323	-66:05:17.85	17.16	4,567±157	0.75±0.35	2.50±0.27	-3.09±0.17

Stellar parameters and metallicities of our low-metallicity LMC stars. *g* is the SkyMapper magnitude as inferred from the Gaia XP spectra. *T_{eff}* (K), log(g), *v_{mic}* and [Fe/H] list the effective temperature, surface gravity, microturbulence parameter and metallicity of the stars, with their respective random uncertainties.

distance of ~1 to ~3 Mpc away from the Milky Way (Methods), at the distance scale of large-scale structure variations in the early Universe²². Star LMC 119, thus, provides a rich opportunity to explore to what extent local first stars differ in their nature across different portions of early large-scale structure through comparisons to analogous Milky Way stars. We fitted the chemical abundances of LMC 119 using population III supernova yield models from ref. ²³, finding that they are reproduced by supernovae with progenitor masses between 10 and 50 times the mass of the Sun and explosion energies up to 4×10^{51} ergs (Methods). The chemical composition of LMC 119 broadly aligns with what is seen in second-generation Milky Way halo stars (Fig. 2d), except that we found an unusually low carbon abundance for this star ([C/Fe] < 0.3). For reference, ~90% of Milky Way stars with [Fe/H] < -4.0 have [C/Fe] > +0.7 (known as carbon-enhanced metal-poor (CEMP) stars)²⁴. This discrepancy hints at a possible divergence in the production channels of carbon, whose overabundance in the lowest-metallicity Milky Way halo stars is often taken as a characteristic signature of the first stars²⁵. However, there have been recent glimpses that carbon enhancement may not be a universal outcome of early element enrichment: one other [Fe/H] ≈ -4.0 star in a dwarf galaxy²¹ is not carbon-enhanced, nor are stars in the Galactic bulge with higher [Fe/H] (refs. ^{26,27}), as well as a handful of the most metal-deficient Milky Way halo and disk stars^{24,28–30}.

Strikingly, we find that none of our LMC low-metallicity stars are CEMP stars (Fig. 2b and Table 2). This is in tension with the Milky Way halo where carbon enhancement is frequent (25% when [Fe/H] < -2.5)³¹. There is a 6% probability that an unbiased sample of ten stars below [Fe/H] = -2.5 would show no carbon enhancement. To further investigate this discrepancy, we observed an additional 15 stars in the LMC, of which eight had [Fe/H] < -2.5, with short exposures to solely derive [Fe/H] and [C/Fe] (Extended Data Table 2). None of these stars are carbon-enhanced either (Methods). Combining these samples leads to a <1% probability of finding no stars that are carbon-enhanced below [Fe/H] = -2.5. Although the selection may have missed the most C-enhanced stars in the LMC with [C/Fe] > 1.3 (Methods), this analysis suggests that the statistical frequency of stars with [C/Fe] > 0.7 through [C/Fe] ≈ 1.3 is lower than that of the Milky Way. The lack of this carbon-enhanced tail of the distribution suggests that some sites of high carbon production (for example, faint supernovae³² and winds of fast-rotating massive stars³³) in the early Milky Way ecosystem may not have been nearly as dominant in the LMC.

Other distinct LMC chemical abundance ratios demonstrate additional differences from equivalent ratios found in the Milky Way and its satellite galaxies. First, the LMC appears to have had strikingly inefficient early star formation or inflows of gas, affirming evidence from

its more metal-rich stars^{9,15} based on the abundances of its α elements (for example, Mg and Ca) as a function of Fe abundance. The downturn in this trend traces the efficiency of star formation (Methods). Combining our LMC sample with data from the literature, we modelled this downturn with a simple linear model, finding that the initial decline occurs at [Fe/H] < -1.82. This is markedly lower than the location of the downturn in the Milky Way ([Fe/H] > -1.0; ref. ³⁴) and what would be expected given the LMC's mass ([Fe/H] ≈ -1.2; ref. ⁹). Interestingly, this is comparable to other Milky Way satellites that are three to five orders of magnitude less massive^{35,36} than the LMC (Fig. 2a,b). Second, previous work on the LMC noted that stars with -2.5 < [Fe/H] < -1.5 were over-enhanced in europium and other elements produced by the rapid (r-) neutron-capture process¹⁵. We found no evidence for europium enhancement ([Eu/Fe] > 0.7) in any of our low-metallicity stars (Fig. 2c), in contrast to the LMC sample with [Fe/H] > -2.5. A probable explanation is that r-process events occurred in the LMC but only at a delayed time once its gas had been enriched to [Fe/H] ≈ -2.5. This is consistent with inefficient star formation, which may lessen the likelihood that rare sites of r-process nucleosynthesis are produced at the lowest metallicities due to the slower stellar mass production¹⁵. The qualitative behaviour of our low-metallicity sample is like that of a recent study of LMC stars with -3.15 < [Fe/H] < -2.45, published after this manuscript was accepted in principle¹⁷. The collectively observed differences thus point to the notable diversity of early chemical and galactic evolution scenarios. After all, the LMC inhabited a qualitatively distant local environment in its early evolution.

We have found intriguing glimpses that a subset of our stars may have been accreted into the LMC from smaller progenitor systems. This confirms previous suggestions of mass assembly using globular cluster data³⁷. We computed the proper motion of our stars relative to the reference frame of the LMC on the plane of the sky and found that 8/10 are rotating directionally with the bulk motion of the galaxy but that 2/10 are counter-rotating (Extended Data Fig. 1). One way to form counter-rotating stars is through accretion events or a collision with the Small Magellanic Cloud^{38,39}, and future work may use the chemistry of lowest-metallicity stars in the Magellanic Cloud ecosystem as a whole to investigate processes arising from past encounters between the Large and Small Magellanic Clouds. Additionally, a handful of our stars also show a deficiency in barium and strontium ([Ba/Fe] ≈ -1.0 and [Sr/Fe] ≈ -1.0), which is an elemental signature typically seen in stars that formed in smaller, ultra-faint dwarf galaxies⁴⁰. Regardless, these stars probe gas from the early ecosystem of the LMC, as preserved by the chemically pristine stars in its own stellar halo. This showcases the powerful insights to be gained from extending the galactic stellar archaeology framework to the LMC to unveil the assembly of its halo.

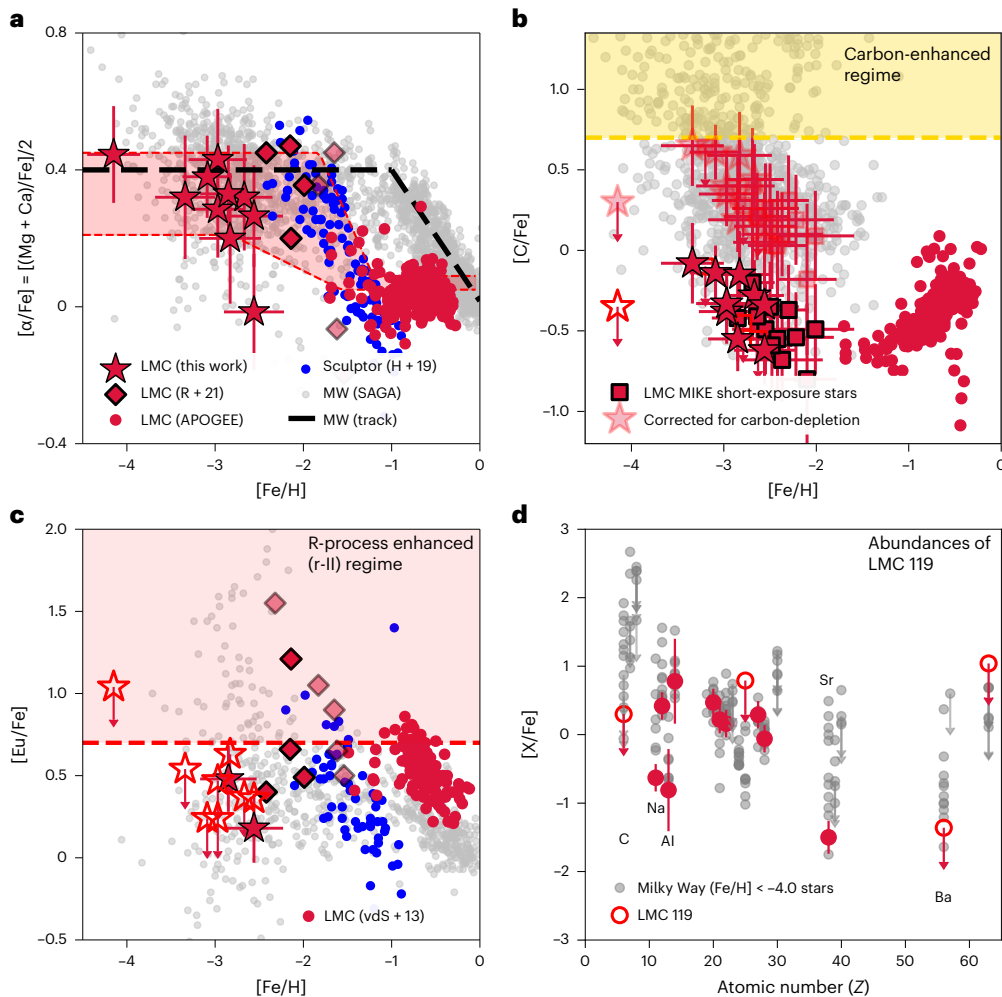


Fig. 2 | Elemental abundance trends of stars in the LMC versus the Milky Way and the Sculptor dwarf galaxy. **a**, The combined trend of the α -element abundance for the LMC is shown in red, for Sculptor in blue³⁶ and for Milky Way (MW) stars in the SAGA database in grey⁸⁶. The α -element track of the Milky Way³⁴ is shown as a dashed line. Red stars correspond to elemental abundances presented in this study, red diamonds correspond to those from ref. 15 and red circles correspond to those from the APOGEE survey^{9,85}. Transparent diamonds correspond to stars in ref. 5 with very cool effective temperatures ($<4,300$ K), which may be susceptible to systematic effects (for example, non-local thermodynamic equilibrium). The red shaded region is the 2σ range of LMC α -knee fits consistent with the data (Methods). Data are presented as mean values \pm standard deviations. Error bars in **b–d** correspond to 1σ random uncertainties, as derived in Methods and shown in Table 2, with N corresponding to the number of absorption features listed in Supplementary Data 2. **b**, Carbon

abundances as a function of [Fe/H] for LMC and Milky Way stars, with the same labelling scheme as in **a**. Lighter stars correspond to our MIKE data after applying a correction for the evolutionary state of carbon following ref. 31. The yellow region corresponds to the regime at which stars are considered to be CEMP stars. The Milky Way compilation is from the SAGA and JINAbase compilation in ref. 24. **c**, Europium (Eu) abundances as a function of metallicity for LMC and Milky Way stars following the labelling scheme in **a**, except the red circles, which are LMC measurements from ref. 92. **d**, Chemical abundances of LMC 119 (the lowest-metallicity LMC star) as a function of atomic number are shown in red, with abundances from Milky Way halo red giant stars from the SAGA database with $[Fe/H] < -4.0$ in grey. The carbon abundance is corrected for the evolutionary state of the star following ref. 31, and we applied the same correction to the compilation in the SAGA database.

Given the high success rate in finding lowest-metallicity stars in the LMC (Methods), our largest satellite galaxy is now a new frontier for stellar archaeology and has extended this field to extragalactic scales.

Methods

Target selection and observations

We identified low-metallicity members of the LMC using DR3 of the Gaia astrometric mission. Specifically, Gaia DR3 provided low-resolution flux-calibrated spectra for ~200 million stars (hereafter known as XP spectra)¹³. The Gaia mission also provided a Python toolkit (GaiaXPy) for computing the photometry for a set of provided imaging filter passbands through these XP spectra. We used this toolkit to derive photometry of these stars through the SkyMapper u, v, g and i filters, and the narrowband CaHK filter centred on 393.3 nm. Previous work

has shown that photometry with these filters can reliably identify stars in the lowest-metallicity regimes^{11,12,41}.

We obtained metallicities for these 200 million XP spectra by matching the inferred SkyMapper u, v, g and i photometry and CaHK photometry from GaiaXPy to a grid of forward-modelled synthetic photometry from synthetic stellar spectra spanning a range of metallicities ($-4.0 < [Fe/H] < -0.5$) on the red giant branch. This XP metallicity catalogue and the details of this implementation will be presented in M.M., A.C. and A.F. (manuscript in preparation), but we describe the relevant details here. This grid of synthetic spectra and photometry was adopted from refs. 14,42, which was generated using the Turbospectrum radiative transfer code^{43,44}, the VALD line list supplemented by updated molecular band information^{45–51} and the MARCS model atmospheres⁵². The synthetic photometry was derived from these

Table 2 | Radial velocities and selected elemental abundances of our low-metallicity LMC stars with high-resolution Magellan/MIKE spectra

Name	RV (km s ⁻¹)	[Fe/H]	[C/Fe]	[C/Fe] _c	[Mg/Fe]	[Ca/Fe]	[Eu/Fe]
LMC 003	281.5±2.0	-2.97±0.20	-0.38±0.20	0.35±0.20	0.38±0.20	0.19±0.20	<0.24
LMC 100	289.0±2.0	-2.67±0.22	-0.28±0.22	0.44±0.22	0.39±0.22	0.25±0.22	<0.37
LMC 104	224.5±2.0	-2.56±0.21	-0.62±0.21	0.15±0.21	0.34±0.21	0.19±0.21	0.18±0.21
LMC 109	222.5±2.0	-2.85±0.20	-0.55±0.20	0.19±0.20	0.43±0.20	0.23±0.20	0.48±0.20
LMC 119	300.7±2.0	-4.15±0.20	<-0.35	<0.30	0.42±0.20	0.47±0.20	<1.04
LMC 124	284.2±2.0	-2.97±0.21	-0.33±0.21	0.40±0.21	0.49±0.21	0.37±0.21	<0.47
LMC 204	252.3±2.0	-2.83±0.27	-0.15±0.27	0.59±0.27	0.31±0.27	0.09±0.27	<0.63
LMC 206	277.2±2.0	-2.56±0.24	-0.34±0.24	0.05±0.24	-0.05±0.24	0.02±0.24	<0.36
LMC 207	334.0±2.0	-3.34±0.25	-0.12±0.25	0.65±0.25	0.16±0.26	0.48±0.25	<0.54
LMC 215	299.6±2.0	-3.09±0.17	-0.14±0.17	0.61±0.17	0.48±0.17	0.28±0.17	<0.24

RV is the heliocentric radial velocity of each star, [Fe/H] is the metallicity, [C/Fe] is the carbon abundance derived from the spectra and [C/Fe]_c is the carbon abundance after correcting for the evolutionary state of the star following ref. 12. [Mg/Fe], [Ca/Fe] and [Eu/Fe] are the magnesium, calcium and europium abundances, respectively. The uncertainties listed here are random uncertainties; the full chemical abundances of these stars, abundances derived from individual absorption features and uncertainties are provided in Supplementary Data 1 and 2.

spectra following refs. 14,42 to generate contours in colour–colour space of constant metallicity. The location of the XP-based photometry in the SkyMapper ($v - g$) – 0.9 × ($g - i$) versus $g - i$ space relative to these contours was used to derive a metallicity (Fig. 3 in ref. 14). The same procedure was applied to derive a metallicity from the CaHK filter using the colour terms (CaHK – g) – 0.9 × ($g - i$) versus ($g - i$). This process provided two estimates of the metallicity for each XP spectrum. For completeness, note that the surface gravity of each star was fixed to the value derived from comparing its location in the absolute g magnitude versus $g - i$ space to Dartmouth isochrones⁵³. If this process for deriving surface gravities did not converge, stars were assigned a surface gravity of $\log g = 2.0$. We used the two metallicity values ([Fe/H]_{SkyMapper XP} and [Fe/H]_{CaHK XP}) to select candidates.

From this global catalogue of XP spectrum-based photometry and metallicities, we selected all stars within 10° of the LMC and applied a number of quality and selection cuts to ensure a pure sample of low-metallicity LMC member stars. First, we removed stars in regions of high reddening ($E(B - V) > 0.2$ in the dust maps from ref. 54). Then, we excluded stars that failed to meet the quality criteria listed in the Gaia XP spectra paper (renormalized unit weight error > 1.4 and $c. < 3$)¹³. We retained stars with reasonable precision in their synthetic SkyMapper v and CaHK magnitudes (<0.2 mag uncertainty). This effectively limited our sample to SkyMapper $g < 17.4$. Next, stars were selected to have proper motions consistent within 2σ of the proper motion distribution of LMC stars¹⁰ and to have locations consistent within 0.1 mag of a [Fe/H] = −2.5, 12 Gyr Dartmouth isochrone⁵³ placed at a distance modulus of 18.5 (ref. 55). The procedure outlining this selection is shown in Fig. 1.

We observed our targets with Magellan/MIKE over three blocks of nights: 30 November and 1 December 2022, 19 December and 20 December 2022, and 27 January 2023. The details of these observations are shown in Extended Data Table 1. The 1.0" slit and 2 × 2 binning were used for all observations, which yielded a wavelength coverage from ~330 to ~900 nm and a resolution of $R \approx 28,000$ over blue wavelengths and $R \approx 22,000$ over the red wavelengths¹⁸. On 30 November, the humidity forced the telescope to close after ~3 h. Snapshot spectra were obtained for a few LMC stars, selected solely based on [Fe/H]_{SkyMapper_XP} < −2.5. This initially resulted in a ~20% success rate (one out of five stars; Extended Data Table 1) of finding stars with [Fe/H] < −2.5. On 1 December, we updated this selection to also require [Fe/H]_{CaHKXP} < −2.5, with a preference given to targets with lower [Fe/H]_{CaHKXP}. This resulted in a 100% success rate of finding stars with [Fe/H] < −2.5. All six stars that were observed were verified to have such low metallicities from their MIKE spectra (LMC 100, LMC 104, LMC 119, LMC 204, LMC 206

and LMC 207). On 19–20 December, three additional low-metallicity stars were observed following the same selection criteria (LMC 109, LMC 124 and LMC 215), and two short-exposure spectra of more metal-rich stars were obtained that passed our selection. Note that LMC 124 was also observed for detailed chemical abundances in ref. 17, published after this paper was accepted in principle. A discussion of the chemical abundances of that star relative to our work is in ‘Chemical abundance analysis of spectra’ (Methods). The 27 January 2023 observations are discussed in the next paragraph.

After an initial analysis of these stars, we noticed that none had a strong CH absorption feature at ~431 nm, indicating a lack of carbon. The SkyMapper passband has a known selection effect against CEMP stars due to the presence of the CN molecular absorption feature in the passband of the SkyMapper v filter (Fig. 2 in ref. 11). This feature makes CEMP stars appear artificially metal-rich in this band, increasing the likelihood that they will be de-selected for a metal-poor star follow-up. A full discussion of this effect is presented in ‘The CEMP fraction and selection effects’ (Methods), but we briefly describe how we actively compensated for this in our January observations here. For the sample observed on 27 January 2023, we opted to obtain MIKE spectra with short exposures to prioritize the deriving of only metallicities and carbon abundances of a larger sample of stars with the same instrumental set-up as before. These stars were selected to have [Fe/H]_{SkyMapper_XP} > −3.0 and [Fe/H]_{CaHK_XP} < −3.0, to proactively select for any CEMP stars, since the narrower CaHK passband is less sensitive to moderately enhanced CN features ([C/Fe] ≈ 0.5; see effect of extreme C enhancement in Fig. 2 in ref. 11). Twelve stars were observed, which all had [Fe/H] < −2.0 (Extended Data Table 2). None were carbon-enhanced. We then observed an additional three stars, selected in the same way, with the medium-resolution ($R \approx 6,000$) Magellan/MagE spectrograph⁵⁶ with the 0.7" slit on 16 March and 17 March 2023 to derive metallicities and carbon abundances. These stars are also listed in Extended Data Table 2.

Note that given the faintness of our targets, the XP metallicity uncertainties were typically >0.5 dex, making our selections closer to a qualitative cut for low-metallicity stars. Due to these large uncertainties arising from source faintness, the metallicities derived from the MIKE spectra show a large scatter around the XP metallicities (systematic offset of 0.27 dex and standard deviation of 0.53 dex).

Chemical abundance analysis of spectra

Three sets of chemical abundance analysis procedures were used to analyse our sample. These corresponded to each of the three subsamples: the long-exposure MIKE spectra for detailed chemical abundances

(in Tables 1 and 2 and Supplementary Data 1 and 2), the short-exposure MIKE data for just metallicities and carbon abundances (in Extended Data Table 2) and the MagE data for metallicities and carbon abundances (also in Extended Data Table 2).

For the sample of long-exposure MIKE spectra, we followed standard stellar chemical abundance analysis methods using ATLAS9 one-dimensional model atmospheres⁵⁷, the 2017 version of the MOOG radiative transfer code^{58,59} and the line list from ref. [60](#). This analysis was performed in the Spectroscopy Made Harder (SMHR) Python wrapper⁶¹, generally following the procedures in refs. [19,62](#), which we briefly describe here. We fitted equivalent widths to derive chemical abundances for each line by fitting a Gaussian profile after local continuum normalization. Initial guesses for the stellar parameters (effective temperature, microturbulence and surface gravity) were based on the location of these stars on the LMC isochrone. Then, these stellar parameters were iteratively adjusted until the Fe I abundances showed no trend with excitation potential and reduced equivalent width. Additionally, the surface gravity was adjusted until the Fe I and Fe II average abundances were in agreement. Then, the temperature correction from ref. [19](#) was applied to bring the temperature scale in line with photometric values, and the microturbulence and surface gravities were again adjusted until the Fe I abundances showed no trend with reduced equivalent width and the Fe I and Fe II average abundances agreed. The chemical abundances from molecular bands or dense regions of absorption features were inferred by fitting synthetic spectra to those regions of the spectrum and varying the abundance of the element of interest.

The final chemical abundances and uncertainties for the long-exposure sample were computed following ref. [62](#) exactly, which we outline here. The final chemical abundance was taken as the mean abundance from individual absorption features of that element. For elements with more than nine absorption features, the standard deviation of the abundances was taken as the random uncertainty. For elements with two to nine absorption features, the random uncertainties were computed by multiplying the range of abundances by the k statistic⁶³. For elements with one absorption feature, the uncertainty was taken as the abundance uncertainty inferred from the parameters fitted to the feature. For Si and Al, the absorption features we used were relatively insensitive to the abundances for these stellar parameters, so an uncertainty floor of 0.55 dex was added to those particular abundances. The random uncertainties on the stellar parameters were taken to correspond to the allowable range from the scatter in the Fe I line trends with excitation potential and reduced equivalent width and the Fe I and Fe II abundances. These random uncertainties were added in quadrature to the systematic uncertainty in the stellar parameters, which were taken to be fiducial values of 150 K in effective temperature, 0.3 dex in surface gravity and 0.2 km s⁻¹ in microturbulence following ref. [62](#). The shifts from varying the stellar parameters by their uncertainties and re-deriving chemical abundances were assumed to be the systematic uncertainties of the chemical abundances. These were added to the random uncertainties of the chemical abundances in quadrature to derive the final chemical abundance uncertainties. For features with no detected lines, 3σ upper limits from a spectrum synthesis were reported. The full chemical abundances and associated uncertainties of this sample are provided in Supplementary Data 1 and 2, and the suite of chemical abundances are plotted in Supplementary Fig. 2.

Note that one star in our sample (LMC 124) has detailed abundances published in ref. [17](#). The elemental abundances agree well, with all [X/Fe] within 1σ with the exception of [Co/Fe], which is discrepant by 0.47 dex (-2σ when accounting only for random uncertainties). Our [Al/Fe] and [Si/Fe] are also discrepant by ~ 0.4 dex, but this is readily explained by the large uncertainties (~ 0.6 dex) on those abundances in our work.

For the short-exposure MIKE data, the same procedure as above was applied with a few notable exceptions. First, the stellar parameters

were fixed to the value inferred from the location of these stars on a 12 Gyr, [Fe/H] = -2.0 Dartmouth isochrone⁵³. This was done since too few Fe I lines were detected in each spectra to robustly constrain the stellar parameters. The uncertainties in these stellar parameters were taken to be the fiducial uncertainties above. Second, the line list for the Fe I lines was chosen to be from the RPA2k line list provided with the Payne4MIKE code, which includes a clean selection of lines from stars based on stars analysed by the R-process Alliance^{64–67}. Third, the carbon abundance was derived only from the CH absorption band at 431 nm. The iron abundance and carbon abundances for these stars are reported in Extended Data Table 2.

For the MagE spectra, the stellar parameters were derived following the same procedure as for the short-exposure MIKE data. The metallicities were derived from the Ca, H and K lines using the well-established KP calibration^{68,69}, implemented following refs. [70,71](#). The carbon abundances were derived using a spectrum synthesis, again following ref. [71](#), which replicated this analysis on similar low-metallicity stars in the Sagittarius dwarf spheroidal galaxy.

Orbit integration to confirm membership

Note that although all of our stars fall within the proper motion and radial velocity criteria for membership of the LMC following ref. [9](#), a few stars have proper motion vectors antiparallel to the bulk motion of nearby LMC members in the centre-of-mass reference frame of the LMC. To ensure that our low-metallicity stars are, in fact, members of the LMC, we integrated their orbits backwards in time to check whether they are gravitationally bound to the LMC. We used the public code in ref. [20](#), which includes the Milky Way, LMC and the Sagittarius dwarf galaxy, and assumed the LMC stars are at a distance of 50 kpc. As shown in Extended Data Fig. 1a, these stars have been bound to the LMC, confirming that they are probably members.

Analysis of the distance between the LMC and Milky Way at high redshifts

We estimated the distance between the LMC and the Milky Way by analysing a suite of cosmological simulations from the Caterpillar Project⁷². The Caterpillar Project includes 32 dark-matter-only zoom-in Milky Way mass halo simulations. Among the satellite dwarfs in these simulations, we selected the most LMC-like satellites by identifying, for each simulation, the most recently accreted or infalling halo with a peak mass ratio between 1:10 to 1:4 compared to the Milky Way mass halo. We also required that they had reached peak mass and began infalling into the Milky Way at $z < 1$. This produced 18 LMC-like halos. After identifying the most LMC-like halos, we traced both their history and the history of the Milky Way mass halo through the simulation back to redshifts $z \approx 6$ to $z \approx 9$, the ages we expect the halo to be forming stars with [Fe/H] = -4.0 to [Fe/H] = -2.5 , following refs. [73,74](#). We calculated the physical distance between the LMC and the Milky Way between these points in time, finding that the distances range from 1 and 3 comoving Mpc. This isolated the early LMC from ejecta from the first stars that formed in the early Milky Way⁷⁵ and placed the LMC at the scale of large-scale structure variations in the early Universe²².

For completeness, note that there are scenarios in the literature in which the LMC is on a second passage (for example, ref. [76](#), and as discussed for an unlikely low-mass LMC in ref. [77](#)). In the scenario in ref. [76](#), the previous pericentric passage of the LMC could have occurred 5–10 Gyr ago but at a large distance of > 100 kpc. In Fig. 4 of ref. [76](#), the distance between the LMC and the Milky Way in this second-infall scenario ~ 11 Gyr ago appears to still be quite far ($\gtrsim 400$ kpc). This is still sufficiently distant for the LMC ecosystem to be shielded from the ejecta of the first stars formed in the Milky Way ecosystem^{78,79}.

Fitting the supernova yield

The most metal-poor star in our sample, LMC 119, is plausibly a second-generation star due to its low metallicity^{5–7}. Consequently, we

fitted its chemical abundance pattern using supernova yield models of the first stars from ref. 23 following the procedure in ref. 80. Briefly, we used fits from these models to estimate the distribution of preferred progenitor star masses, supernova explosion energy and dilution mass following a chi-squared fitting procedure to the chemical abundance pattern of LMC 119. We found that a broad range of masses ($10 M_{\odot}$ to $50 M_{\odot}$), explosion energies (up to 4×10^{51} ergs) and dilution masses ($10^5 M_{\odot}$ to $10^{6.5} M_{\odot}$) are consistent with the abundance pattern of LMC 119. Note that only C, Na, Mg, Ca, Ti, Fe, Co and Ni were included in this analysis due to a combination of their relatively lower abundance uncertainties and upper limits and their somewhat lower sensitivity to non-local thermodynamic equilibrium effects than other elemental abundances. The results of this fitting procedure are shown in Supplementary Fig. 3.

α-knee fitting

Abundances of α elements (for example, Mg and Ca) as a function of [Fe/H] trace the efficiency of star formation. This is because core-collapse supernovae dominate early metal production and over-produce these elements ($[\alpha/\text{Fe}] \approx 0.4$; ref. 81). Type Ia supernovae occur after some delay time⁸² and produce only traces of α elements⁸³ but notable amounts of iron-peak elements (for example, Fe, Ni and Mn). Consequently, the [Fe/H] at which $[\alpha/\text{Fe}]$ starts to decline maps onto the early star formation efficiency. We modelled the location of the downturn in the α-element abundances (the α knee) as a function of [Fe/H] largely following ref. 84, which we outline here. First, we took $[\alpha/\text{Fe}] = ([\text{Mg}/\text{Fe}] + [\text{Ca}/\text{Fe}])/2$, as these two α elements are typically those with the smallest uncertainties. We modelled the trend of $[\alpha/\text{Fe}]$ versus [Fe/H] as a piecewise linear model with four parameters: $[\alpha/\text{Fe}]$ (high), which is the average $[\alpha/\text{Fe}]$ value at the low-metallicity end; [Fe/H] (low), which indicates the metallicity at which $[\alpha/\text{Fe}]$ starts declining; [Fe/H] (high), which indicates the metallicity at which $[\alpha/\text{Fe}]$ stops declining; and $[\alpha/\text{Fe}]$ (low), which is the constant $[\alpha/\text{Fe}]$ value at the high-metallicity end.

We fitted the above model to a compilation of LMC data from refs. 9, 15, 85 and our sample of low-metallicity LMC stars. The fitting was performed using the `scipy curve_fit` function, while allowing $[\alpha/\text{Fe}]$ (high) and $[\alpha/\text{Fe}]$ (low) to vary by 0.2 dex around the mean $[\alpha/\text{Fe}]$ of stars with $[\text{Fe}/\text{H}] < -3.0$ and $[\text{Fe}/\text{H}] > -1.0$, respectively. Additionally, $[\text{Fe}/\text{H}]$ (high) was allowed to vary between -2.0 and -0.5 , and $[\text{Fe}/\text{H}]$ (low) was allowed to vary between -3.0 and -1.0 . Then, the LMC data compilation was resampled 10,000 times based on the chemical abundance uncertainties and the same parameters were re-derived each time. The standard deviation of the resulting parameter distribution was taken as the random uncertainty of the parameter values. This random uncertainty in the model fit was added to the errors inferred from the covariance matrix returned by `curve_fit` in quadrature to derive the final uncertainty value for each of these parameters. Notably, with $[\text{Fe}/\text{H}]$ (low), we constrained the location of the α knee to $[\text{Fe}/\text{H}] < -1.82$, substantially lower than what would be expected ($[\text{Fe}/\text{H}] \approx -1.2$; ref. 9) for a galaxy with the mass of the LMC³⁴. Visually, this low downturn is also evident in Fig. 2a and in the individual $[\text{Ca}/\text{Fe}]$ and $[\text{Mg}/\text{Fe}]$ trends when combined with literature samples. The fits to the parameters are as follows: $[\alpha/\text{Fe}]$ (high) = 0.33 ± 0.06 , $[\text{Fe}/\text{H}]$ (high) = -1.39 ± 0.09 , $[\alpha/\text{Fe}]$ (low) = 0.07 ± 0.01 and $[\text{Fe}/\text{H}]$ (low) = -2.32 ± 0.25 . We emphasize that we report the latter fit in terms of its 2σ upper limit when discussing the α knee due to the visually highly uncertain location of the specific downturn in $[\alpha/\text{Fe}]$ (Fig. 2a). Excluding the cool stars ($<4,300$ K) in ref. 15 shifts the location of the above fits by less than 0.1 dex. Fully excluding the stars in ref. 15 leads to an artificially low α knee of $[\text{Fe}/\text{H}] = -2.73$, as the stars in ref. 15 are largely in the metallicity range between $[\text{Fe}/\text{H}] > -2.5$ and $[\text{Fe}/\text{H}] < -2.0$. Excluding our new low-metallicity sample led to a fit that did not converge.

Note that we used this simple piecewise linear model only to gain insights about the approximate initial downturn of the α knee.

This model is probably insufficient to explain the full morphology of the trend. Accordingly, the exact parameters of this model should not be assumed to fully represent the LMC α track. A more complete description of the LMC α-element evolution can be obtained for $[\text{Fe}/\text{H}] > -2.2$ in the b-spline fits in Fig. 14 of ref. 9.

The CEMP fraction and selection effects

The CEMP fraction in our sample was taken as the fraction of stars with $[\text{C}/\text{Fe}]_c > 0.7$ divided by the total number of stars, which allowed a consistent comparison to Milky Way carbon-enhanced fractions reported in the literature³¹. Note that the carbon abundances that were derived from the spectra were corrected for the evolutionary state of the star following ref. 31. This is because stars deplete carbon in their photospheres as they ascend the red giant branch, so this correction was applied to recover their natal abundance of carbon. Since all of our LMC stars are well ascended on the red giant branch, their carbon corrections are often large (-0.5 to -0.7 dex), as seen in Table 2 and Extended Data Table 2.

Given the low carbon abundances of the low-metallicity stars that we detected in the LMC, we performed several checks to ensure that a biased target selection could not reasonably explain the carbon deficiency. In particular, these stars were flagged as low-metallicity candidates due to their brightness in the metallicity-sensitive filter covering the Ca II, H and K absorption feature at 393 nm. There is a prominent CN absorption band bluewards of this feature (at ~385 nm), which can make stars appear faint (and, thus, more metal-rich), if the carbon abundance is sufficiently high. However, the strength of this spectral feature depends on several quantities, for example, the effective temperature of the star, its carbon and nitrogen abundances, and its metallicity. Importantly, the evolutionary state of the star affects the surface carbon and nitrogen abundance and also influences the strength of this CN feature. The strength of the band increases with decreasing temperature, increasing metallicity and increasing carbon abundance. Additionally, the carbon-enhanced threshold (corrected $[\text{C}/\text{Fe}] > 0.7$) for our stars would generally be met already when the inferred morphology of the CN band is fairly weak (for example, corresponding to uncorrected $[\text{C}/\text{Fe}] \approx 0$), due to the large corrections for carbon depletion for stars on the red giant branch.

Accordingly, the effect of our selection function had to be assessed using a sample of stars spanning similar metallicities, effective temperatures and surface gravities. We queried the SAGA database of metal-poor stars for stars⁸⁶ with effective temperatures $<4,750$ K and $\log g < 2.0$ to match our sample of LMC stars. We then cross-matched this compilation with our XP catalogue of metallicities. We replicated our selection function for the LMC stars on this cross-matched catalogue. Specifically, all ten of our long-exposure LMC stars had $[\text{Fe}/\text{H}]_{\text{CaHKXP}} < -2.8$ and $[\text{Fe}/\text{H}]_{\text{SkyMapperXP}} < -3.0$. We computed the fraction of stars below $[\text{Fe}/\text{H}] < -2.5$ in SAGA that are above various uncorrected $[\text{C}/\text{Fe}]$ thresholds before and after applying these selection criteria. Notably, we found no meaningful difference in the recovered fraction of stars with $[\text{C}/\text{Fe}] > 0.0$ before ($N = 23$ and fraction 0.36) and after ($N = 11$ and fraction 0.34) applying our selection, implying that we ought to have found stars with uncorrected $[\text{C}/\text{Fe}] > 0$ in an unbiased manner in the metallicity regime considered for this study. None of the LMC stars have uncorrected $[\text{C}/\text{Fe}] > 0.0$, as shown in Table 2 or Extended Data Table 2. Note that none of the three most carbon-enhanced stars in SAGA (all with uncorrected $[\text{C}/\text{Fe}] > 0.65$) in this metallicity regime were recovered by our selection. Consequently, we are biased against the most drastically carbon-enhanced stars in the LMC, which is consistent with previous work showing a selection against copious carbon enhancement by these photometric filters^{11,14,41,87}. However, as shown by the SAGA analysis, we see no evidence for a bias against moderately carbon-enhanced stars for the stellar parameter and metallicity regime in this study, in the carbon regime where we do not readily see these

stars in our LMC sample. An uncorrected $[C/Fe] > 0$ roughly maps to $[C/Fe] > 0.7$ after applying carbon corrections for the typical stellar parameters of our sample. Note that the short-exposure MIKE and MagE sample would be less susceptible to the biases discussed here since they were chosen to have $[Fe/H]_{\text{SkyMapper XP}} > -3.0$ ('Target selection and observations' in Methods).

Note that, generally, the most carbon-enhanced stars (for example, uncorrected $[C/Fe] > 1.0$) can also appear meaningfully redder than the adopted isochrone for target selection, leading to a potential exclusion from our selection in Fig. 1b. For example, ref. 88 recently identified a very metal-poor, extremely carbon-enhanced star ($[Fe/H] = -2.5$ and $[C/Fe] \approx 2.5$) in Reticulum II that was 0.25 mag redder than the isochrone overplotted in their Fig. 1. We probably excluded such stars from our selection in the LMC due to the 0.1 mag range of our isochrone selection. However, as also seen in Fig. 1 of ref. 88, the other stars in Reticulum II track the isochrone closely and have corrected carbon abundances spanning $[C/Fe] = 0.16$ to 1.29 (ref. 89). Consequently, our isochrone selection principally excludes extremely carbon-enhanced stars in the LMC but ought to have still selected stars well beyond the CEMP threshold ($[C/Fe] > 0.7$), as shown in and spanning the y axis in Fig. 2b. Such extremely carbon-enhanced stars, when they show no enhancement in elements produced by the slow neutron-capture process (s-process), are known as group III stars⁹⁰. We could not identify such stars in our selection while it was still sensitive to so-called group II carbon-enhanced stars, which show a less drastic carbon enhancement⁹⁰ still above the $[C/Fe] > 0.7$ threshold.

We also tested to see whether our sample indicates differences in the mean carbon abundance versus $[Fe/H]$ relative to the Milky Way, as opposed to just a differing fraction of stars that are carbon-enhanced ($[C/Fe] > 0.7$). We divided our LMC sample into bins of 0.5 dex in $[Fe/H]$ from -2.0 to -3.5 and computed the mean $[C/Fe]$ in each of these to compare with the Milky Way halo. We found that the mean carbon abundance of the LMC sample is consistent with the Milky Way halo trend (ranging from 0.03 to 0.18 dex below the Milky Way median values), despite the lack of CEMP stars in our LMC sample. This analysis, however, is heavily caveated by the small number of LMC stars (two to 11 stars) in each metallicity bin.

Data availability

The velocities and chemical abundances derived from the long-exposure MIKE spectra in this study are presented in Table 2 and Supplementary Data 1. Abundance measurements for individual absorption features in these stars are provided in Supplementary Data 2. We report short-exposure MIKE and MagE metallicities and carbon abundances in Extended Data Table 2. The stellar spectra of these stars are available from the corresponding author upon request. The proper motions of these stars are available from the Gaia data archive (<https://gea.esac.esa.int/archive/>). The data tables will be posted in machine-readable format at Zenodo <https://doi.org/10.5281/zenodo.10032360> upon publication⁹¹. Source data are provided with this paper.

Code availability

The stellar synthesis code MOOG that was used to analyse these data can be retrieved from <https://github.com/alexji/moog17scat>. The analysis package SMHR that wraps around MOOG can be retrieved from <https://github.com/andycasey/smhr>. The orbit integration code that includes the Milky Way, LMC and Sagittarius can be retrieved from ref. 20. The Payne4MIKE code used to analyse the short-exposure MIKE spectra can be retrieved from <https://github.com/tingyuansen/Payne4MIKE>. The chemical abundance analysis of the two MagE spectra was performed using the authors' implementations of published techniques, which are straightforward to reproduce from the publications, but are available from the corresponding author upon request.

References

- Shipp, N. et al. Measuring the mass of the Large Magellanic Cloud with stellar streams observed by S⁵. *Astrophys. J.* **923**, 149 (2021).
- Koposov, S. E. et al. S⁵: probing the Milky Way and Magellanic Clouds potentials with the 6-D map of the Orphan-Chenab stream. *Mon. Not. R. Astron. Soc.* **521**, 4936–4962 (2023).
- Besla, G. et al. Are the Magellanic Clouds on their first passage about the Milky Way? *Astrophys. J.* **668**, 949–967 (2007).
- Conroy, C. et al. All-sky dynamical response of the Galactic halo to the Large Magellanic Cloud. *Nature* **592**, 534–536 (2021).
- Frebel, A. & Norris, J. E. Near-field cosmology with extremely metal-poor stars. *Annu. Rev. Astron. Astrophys.* **53**, 631–688 (2015).
- Cayrel, R. et al. First stars. V. Abundance patterns from C to Zn and supernova yields in the early Galaxy. *Astron. Astrophys.* **416**, 1117–1138 (2004).
- Ji, A. P., Frebel, A. & Bromm, V. Preserving chemical signatures of primordial star formation in the first low-mass stars. *Mon. Not. R. Astron. Soc.* **454**, 659–674 (2015).
- The Gaia Collaboration. Gaia Data Release 3: summary of the content and survey properties. *Astron. Astrophys.* **674**, A1 (2023).
- Nidever, D. L. et al. The lazy giants: APOGEE abundances reveal low star formation efficiencies in the Magellanic Clouds. *Astrophys. J.* **895**, 88 (2020).
- The Gaia Collaboration. Gaia Early Data Release 3: structure and properties of the Magellanic Clouds. *Astron. Astrophys.* **649**, A7 (2021).
- Starkenburg, E. et al. The Pristine survey. I. Mining the Galaxy for the most metal-poor stars. *Mon. Not. R. Astron. Soc.* **471**, 2587–2604 (2017).
- Keller, S. C. et al. The SkyMapper Telescope and the Southern Sky Survey. *Publ. Astron. Soc. Aust.* **24**, 1–12 (2007).
- The Gaia Collaboration. Gaia Data Release 3: the Galaxy in your preferred colours. Synthetic photometry from Gaia low-resolution spectra. *Astron. Astrophys.* **674**, A33 (2023).
- Chiti, A., Frebel, A., Jerjen, H., Kim, D. & Norris, J. E. Stellar metallicities from SkyMapper photometry. I. A study of the Tucana II ultra-faint dwarf galaxy. *Astrophys. J.* **891**, 8–31 (2020).
- Reggiani, H., Schlaufman, K. C., Casey, A. R., Simon, J. D. & Ji, A. P. The most metal-poor stars in the Magellanic Clouds are r-process enhanced. *Astron. J.* **162**, 229 (2021).
- Oh, W. S., Nordlander, T., Da Costa, G. S., Bessell, M. S. & Mackey, A. D. The SkyMapper search for extremely metal-poor stars in the Large Magellanic Cloud. *Mon. Not. R. Astron. Soc.* **524**, 577–582 (2023).
- Oh, W. S., Nordlander, T., Da Costa, G. S., Bessell, M. S. & Mackey, A. D. High-resolution spectroscopic study of extremely metal-poor stars in the Large Magellanic Cloud. *Mon. Not. R. Astron. Soc.* **528**, 1065–1080 (2024).
- Bernstein, R., Shectman, S. A., Gunnels, S. M., Mochnacki, S. & Athey, A. E. MIKE: a double echelle spectrograph for the Magellan telescopes at Las Campanas Observatory. *Proc. SPIE* **4841**, 1694–1704 (2003).
- Frebel, A., Casey, A. R., Jacobson, H. R. & Yu, Q. Deriving stellar effective temperatures of metal-poor stars with the excitation potential method. *Astrophys. J.* **769**, 57 (2013).
- Vasiliev, E., Belokurov, V. & Erkal, D. Tango for three: Sagittarius, LMC, and the Milky Way. *Mon. Not. R. Astron. Soc.* **501**, 2279–2304 (2021).
- Skuladottir, A., Vanni, I., Salvadori, S. & Lucchesi, R. Tracing pop III supernovae with extreme energies through the Sculptor dwarf spheroidal galaxy. *Astron. Astrophys.* **681**, A44 (2024).
- Planck Collaboration. Planck 2018 results. VI. Cosmological parameters. *Astron. Astrophys.* **641**, A6 (2020).
- Heger, A. & Woosley, S. E. Nucleosynthesis and evolution of massive metal-free stars. *Astrophys. J.* **724**, 341–373 (2010).

24. Placco, V. M. et al. SPLUS J210428.01-004934.2: an ultra metal-poor star identified from narrowband photometry. *Astrophys. J.* **912**, L32 (2021).
25. Jeon, M., Besla, G. & Bromm, V. Connecting the first galaxies with ultrafaint dwarfs in the Local Group: chemical signatures of population III stars. *Astrophys. J.* **848**, 85 (2017).
26. Howes, L. M. et al. Extremely metal-poor stars from the cosmic dawn in the bulge of the Milky Way. *Nature* **527**, 484–487 (2015).
27. Arentsen, A. et al. The Pristine Inner Galaxy Survey (PIGS) III: carbon-enhanced metal-poor stars in the bulge. *Mon. Not. R. Astron. Soc.* **505**, 1239–1253 (2021).
28. Mardini, M. K. et al. The Atari disk, a metal-poor stellar population in the disk system of the Milky Way. *Astrophys. J.* **936**, 78 (2022).
29. Caffau, E. et al. An extremely primitive star in the Galactic halo. *Nature* **477**, 67–69 (2011).
30. Mardini, M. K. et al. The chemical abundance pattern of the extremely metal-poor thin disc star 2MASS J1808-5104 and its origins. *Mon. Not. R. Astron. Soc.* **517**, 3993–4004 (2022).
31. Placco, V. M., Frebel, A., Beers, T. C. & Stancliffe, R. J. Carbon-enhanced metal-poor star frequencies in the Galaxy: corrections for the effect of evolutionary status on carbon abundances. *Astrophys. J.* **797**, 21 (2014).
32. Tominaga, N., Umeda, H. & Nomoto, K. Supernova nucleosynthesis in population III 13–50 M_{\odot} stars and abundance patterns of extremely metal-poor stars. *Astrophys. J.* **660**, 516–540 (2007).
33. Maeder, A., Meynet, G. & Chiappini, C. The first stars: CEMP-no stars and signatures of spinstars. *Astron. Astrophys.* **576**, A56 (2015).
34. Matteucci, F. & Greggio, L. Relative roles of type I and II supernovae in the chemical enrichment of the interstellar gas. *Astron. Astrophys.* **154**, 279–287 (1986).
35. Reichert, M. et al. Neutron-capture elements in dwarf galaxies. III. A homogenized analysis of 13 dwarf spheroidal and ultra-faint galaxies. *Astron. Astrophys.* **641**, A127 (2020).
36. Hill, V. et al. VLT/FLAMES high-resolution chemical abundances in Sculptor: a textbook dwarf spheroidal galaxy. *Astron. Astrophys.* **626**, A15 (2019).
37. Mucciarelli, A. et al. A relic from a past merger event in the Large Magellanic Cloud. *Nat. Astron.* **5**, 1247–1254 (2021).
38. Olsen, K. A. G., Zaritsky, D., Blum, R. D., Boyer, M. L. & Gordon, K. D. A population of accreted Small Magellanic Cloud stars in the Large Magellanic Cloud. *Astrophys. J.* **737**, 29 (2011).
39. Armstrong, B. & Bekki, K. Formation of a counter-rotating stellar population in the Large Magellanic Cloud: a Magellanic triplet system? *Mon. Not. R. Astron. Soc.* **480**, L141–L145 (2018).
40. Ji, A. P., Simon, J. D., Frebel, A., Venn, K. A. & Hansen, T. T. Chemical abundances in the ultra-faint dwarf galaxies Grus I and Triangulum II: neutron-capture elements as a defining feature of the faintest dwarfs. *Astrophys. J.* **870**, 83 (2019).
41. Da Costa, G. S. et al. The SkyMapper DR1.1 search for extremely metal-poor stars. *Mon. Not. R. Astron. Soc.* **489**, 5900–5918 (2019).
42. Chiti, A. et al. Stellar metallicities from SkyMapper Photometry. II. Precise photometric metallicities of ~280,000 giant stars with $[Fe/H] < -0.75$ in the Milky Way. *Astrophys. J. Suppl. Ser.* **254**, 31 (2021).
43. Alvarez, R. & Plez, B. Near-infrared narrow-band photometry of M-giant and Mira stars: models meet observations. *Astron. Astrophys.* **330**, 1109–1119 (1998).
44. Plez, B. Turbospectrum: Code for spectral synthesis. *Astrophysics Source Code Library ascl:1205.004* (2012).
45. Piskunov, N. E., Kupka, F., Ryabchikova, T. A., Weiss, W. W. & Jeffery, C. S. VALD: The Vienna Atomic Line Data Base. *Astron. Astrophys. Suppl. Ser.* **112**, 525 (1995).
46. Brooke, J. S. A., Bernath, P. F., Schmidt, T. W. & Bacskay, G. B. Line strengths and updated molecular constants for the C_2 Swan system. *J. Quant. Spectrosc. Radiat. Transf.* **124**, 11–20 (2013).
47. Brooke, J. S. A. et al. Einstein A coefficients and oscillator strengths for the $A^2\Pi-X^2\Sigma^+$ (red) and $B^2\Sigma^+-X^2\Sigma^+$ (violet) systems and rovibrational transitions in the $X^2\Sigma^+$ state of CN. *Astrophys. J. Suppl. Ser.* **210**, 23 (2014).
48. Masseron, T. et al. CH in stellar atmospheres: an extensive linelist. *Astron. Astrophys.* **571**, A47 (2014).
49. Sneden, C., Lucatello, S., Ram, R. S., Brooke, J. S. A. & Bernath, P. Line lists for the $A^2\Pi-X^2\Sigma^+$ (red) and $B^2\Sigma^+-X^2\Sigma^+$ (violet) systems of CN, $^{13}C^{14}N$, and $^{12}C^{15}N$, and application to astronomical spectra. *Astrophys. J. Suppl. Ser.* **214**, 26 (2014).
50. Ram, R. S., Brooke, J. S. A., Bernath, P. F., Sneden, C. & Lucatello, S. Improved line data for the Swan system $^{12}C^{13}C$ isotopologue. *Astrophys. J. Suppl. Ser.* **211**, 5 (2014).
51. Ryabchikova, T. et al. A major upgrade of the VALD database. *Phys. Scr.* **90**, 054005 (2015).
52. Gustafsson, B. et al. A grid of MARCS model atmospheres for late-type stars. I. Methods and general properties. *Astron. Astrophys.* **486**, 951–970 (2008).
53. Dotter, A. et al. The Dartmouth Stellar Evolution Database. *Astrophys. J. Suppl. Ser.* **178**, 89–101 (2008).
54. Schlegel, D. J., Finkbeiner, D. P. & Davis, M. Maps of dust infrared emission for use in estimation of reddening and cosmic microwave background radiation foregrounds. *Astrophys. J.* **500**, 525 (1998).
55. Alves, D. R. A review of the distance and structure of the Large Magellanic Cloud. *New Astron. Rev.* **48**, 659–665 (2004).
56. Marshall, J. L. et al. The MagE spectrograph. *Proc. SPIE Int. Soc. Opt. Eng.* **7014**, 54–63 (2008).
57. Castelli, F. & Kurucz, R. L. New grids of ATLAS9 model atmospheres. *Model. Stellar Atmos.* **210**, A20 (2003).
58. Sneden, C. A. *Carbon and Nitrogen Abundances in Metal-Poor Stars*. PhD thesis, Harvard Univ. (1973).
59. Sobeck, J. S. et al. The abundances of neutron-capture species in the very metal-poor globular cluster M15: a uniform analysis of red giant branch and red horizontal branch stars. *Astron. J.* **141**, 175 (2011).
60. Ji, A. P. et al. The Southern Stellar Stream Spectroscopic Survey (S⁵): chemical abundances of seven stellar streams. *Astron. J.* **160**, 181 (2020).
61. Casey, A. R. *A Tale of Tidal Tails in the Milky Way*. Preprint at arxiv.org/abs/1405.5968 (2014).
62. Chiti, A. et al. Detailed chemical abundances of stars in the outskirts of the Tucana II ultrafaint dwarf galaxy. *Astron. J.* **165**, 55 (2023).
63. Kenney, J. F. *Mathematics of Statistics*, 3rd edn (Van Nostrand, 1962).
64. Hansen, T. T. et al. The R-process Alliance: first release from the southern search for r-process-enhanced stars in the Galactic halo. *Astrophys. J.* **858**, 92 (2018).
65. Sakari, C. M. et al. The R-Process Alliance: first release from the northern search for r-process-enhanced metal-poor stars in the Galactic halo. *Astrophys. J.* **868**, 110 (2018).
66. Ezzeddine, R. et al. The R-Process Alliance: first Magellan/MIKE release from the Southern search for r-process-enhanced stars. *Astrophys. J.* **898**, 150 (2020).
67. Holmbeck, E. M. et al. The R-Process Alliance: fourth data release from the search for R-process-enhanced stars in the Galactic halo. *Astrophys. J. Suppl. Ser.* **249**, 30 (2020).
68. Beers, T. C., Rossi, S., Norris, J. E., Ryan, S. G. & Sheffler, T. Estimation of stellar metal abundance. II. A recalibration of the Ca II K technique, and the autocorrelation function method. *Astron. J.* **117**, 981–1009 (1999).

69. Beers, T. C. & Christlieb, N. The discovery and analysis of very metal-poor stars in the Galaxy. *Annu. Rev. Astron. Astrophys.* **43**, 531–580 (2005).
70. Chiti, A. et al. Detection of a population of carbon-enhanced metal-poor stars in the Sculptor dwarf spheroidal galaxy. *Astrophys. J.* **856**, 142 (2018).
71. Chiti, A., Hansen, K. Y. & Frebel, A. Discovery of 18 stars with $-3.10 < [\text{Fe}/\text{H}] < -1.45$ in the Sagittarius dwarf galaxy. *Astrophys. J.* **901**, 164 (2020).
72. Griffen, B. F. et al. The Caterpillar Project: a large suite of Milky Way sized halos. *Astrophys. J.* **818**, 10 (2016).
73. Brauer, K. et al. The origin of r-process enhanced metal-poor halo stars in now-destroyed ultra-faint dwarf galaxies. *Astrophys. J.* **871**, 247 (2019).
74. Pakmor, R. et al. Formation and fate of low-metallicity stars in TNG50. *Mon. Not. R. Astron. Soc.* **512**, 3602–3615 (2022).
75. Smith, B. D., Wise, J. H., O’Shea, B. W., Norman, M. L. & Khochfar, S. The first population II stars formed in externally enriched mini-haloes. *Mon. Not. R. Astron. Soc.* **452**, 2822–2836 (2015).
76. Vasiliev, E. Dear Magellanic Clouds, welcome back! *Mon. Not. R. Astron. Soc.* **527**, 437–456 (2024).
77. Kallivayalil, N., van der Marel, R. P., Besla, G., Anderson, J. & Alcock, C. Third-epoch Magellanic Cloud proper motions. I. Hubble Space Telescope/WFC3 data and orbit implications. *Astrophys. J.* **764**, 161 (2013).
78. Griffen, B. F. et al. Tracing the first stars and galaxies of the Milky Way. *Mon. Not. R. Astron. Soc.* **474**, 443–459 (2018).
79. Magg, M. et al. Predicting the locations of possible long-lived low-mass first stars: importance of satellite dwarf galaxies. *Mon. Not. R. Astron. Soc.* **473**, 5308–5323 (2018).
80. Ji, A. P. et al. Detailed abundances in the ultra-faint Magellanic satellites Carina II and III. *Astrophys. J.* **889**, 27 (2020).
81. Nomoto, K., Tominaga, N., Umeda, H., Kobayashi, C. & Maeda, K. Nucleosynthesis yields of core-collapse supernovae and hypernovae, and galactic chemical evolution. *Nucl. Phys. A* **777**, 424–458 (2007).
82. Maoz, D. & Graur, O. Star formation, supernovae, iron, and α : consistent cosmic and Galactic histories. *Astrophys. J.* **848**, 25 (2017).
83. Tinsley, B. M. Stellar lifetimes and abundance ratios in chemical evolution. *Astrophys. J.* **229**, 1046–1056 (1979).
84. Cohen, J. G. & Huang, W. The chemical evolution of the Ursa Minor dwarf spheroidal galaxy. *Astrophys. J.* **719**, 931 (2010).
85. Abdurro’uf et al. The Seventeenth Data Release of the Sloan Digital Sky Surveys: complete release of MaNGA, MaStar, and APOGEE-2 Data. *Astrophys. J. Suppl. Ser.* **259**, 35 (2022).
86. Suda, T. et al. Stellar Abundances for the Galactic Archeology (SAGA) Database—compilation of the characteristics of known extremely metal-poor stars. *Publ. Astron. Soc. Jpn* **60**, 1159–1171 (2008).
87. Arentsen, A. et al. On the inconsistency of [C/Fe] abundances and the fractions of carbon-enhanced metal-poor stars among various stellar surveys. *Mon. Not. R. Astron. Soc.* **515**, 4082–4098 (2022).
88. Hayes, C. R. et al. GHOST commissioning science results: identifying a new chemically peculiar star in Reticulum II. *Astrophys. J.* **955**, 17 (2023).
89. Ji, A. P., Frebel, A., Simon, J. D. & Chiti, A. Complete element abundances of nine stars in the r-process galaxy Reticulum II. *Astrophys. J.* **830**, 93 (2016).
90. Yoon, J. et al. Observational constraints on first-stars nucleosynthesis. I. Evidence for multiple progenitors of CEMP-no stars. *Astrophys. J.* **833**, 20 (2016).
91. Chiti, A. et al. Data tables for enrichment by extragalactic first stars in the Large Magellanic Cloud. Zenodo <https://doi.org/10.5281/zenodo.10032360> (2024).
92. Van der Swaelmen, M., Hill, V., Primas, F. & Cole, A. A. Chemical abundances in LMC stellar populations. II. The bar sample. *Astron. Astrophys.* **560**, A44 (2013).

Acknowledgements

Our data were gathered using the 6.5 m Magellan Baade telescope at Las Campanas Observatory, Chile. A.C. thanks A. Drlica-Wagner, K. Olsen, D. Nidever, G. Stringfellow, W. Cerny, K. Venn, A. Arentsen, V. Placco, I. Roederer, P. Sharda and A. Kravtsov for helpful discussions, and R. Prasad for their support. A.C. also thanks V. Placco for providing a compilation of corrected carbon abundances of metal-poor Milky Way stars. This work benefited from the KICP/UChicago Gaia DR3 sprint and made use of NASA’s Astrophysics Data System Bibliographic Services, the SIMBAD database (operated at the Strasbourg Astronomical Data Centre, Strasbourg, France) and the open-source Python libraries numpy, scipy, matplotlib and astropy. A.C. is supported by a Brinson Prize Fellowship at the Kavli Institute for Cosmological Physics, University of Chicago. G.L. acknowledges support from the São Paulo Research Foundation (Grant Nos. 2021/10429-0 and 2022/07301-5). A.P.J. acknowledges support from the US National Science Foundation (NSF; Grant Nos. AST-2206264 and AST-2307599). T.S.L. acknowledges financial support from the Natural Sciences and Engineering Research Council of Canada (Grant No. RGPIN-2022-04794). K.B. is supported by an NSF astronomy and astrophysics postdoctoral fellowship (Award No. AST-2303858). H.D.A. acknowledges support from the Undergraduate Research Opportunities Program at the Massachusetts Institute of Technology. This work has made use of data from the European Space Agency’s mission Gaia (<https://www.cosmos.esa.int/gaia>) that has been processed by the Gaia Data Processing and Analysis Consortium (DPAC); <https://www.cosmos.esa.int/web/gaia/dpac/consortium>). Funding for the DPAC has been provided by national institutions, in particular the institutions participating in the Gaia Multilateral Agreement. The national facility capability for SkyMapper has been funded through the Linkage Infrastructure, Equipment and Facilities scheme of the Australian Research Council (Grant No. LE130100104), which was awarded to the University of Sydney, the Australian National University, Swinburne University of Technology, the University of Queensland, the University of Western Australia, the University of Melbourne, Curtin University of Technology, Monash University and the Australian Astronomical Observatory. SkyMapper is owned and operated by the Australian National University’s Research School of Astronomy and Astrophysics.

Author contributions

A.C. designed the technique for generating the Gaia XP metallicity catalogue used in this work, selected candidates for the observations and led the MIKE observations, analysis, interpretation, and paper writing. M.M. generated the Gaia XP metallicity catalogue and assisted with making the MIKE observations and their analysis and interpretation. A.P.J. and G.L. assisted with the analysis, interpretation and paper writing. A.F. assisted with the MIKE observations, interpretation and paper writing. H.R. provided existing MIKE observations of LMC stars and assisted with the interpretation. P.F. generated the catalogue of synthetic Gaia XP photometry. K.B. and H.D.A. led the analysis of the distance of the LMC from the Milky Way when it was producing low-metallicity stars. T.S.L. and J.D.S. led and assisted with the MagE observations. All authors provided feedback on the paper before submission.

Competing interests

The authors declare no competing interests.

Additional information

Extended data is available for this paper at
<https://doi.org/10.1038/s41550-024-02223-w>.

Supplementary information The online version contains supplementary material available at
<https://doi.org/10.1038/s41550-024-02223-w>.

Correspondence and requests for materials should be addressed to Anirudh Chiti.

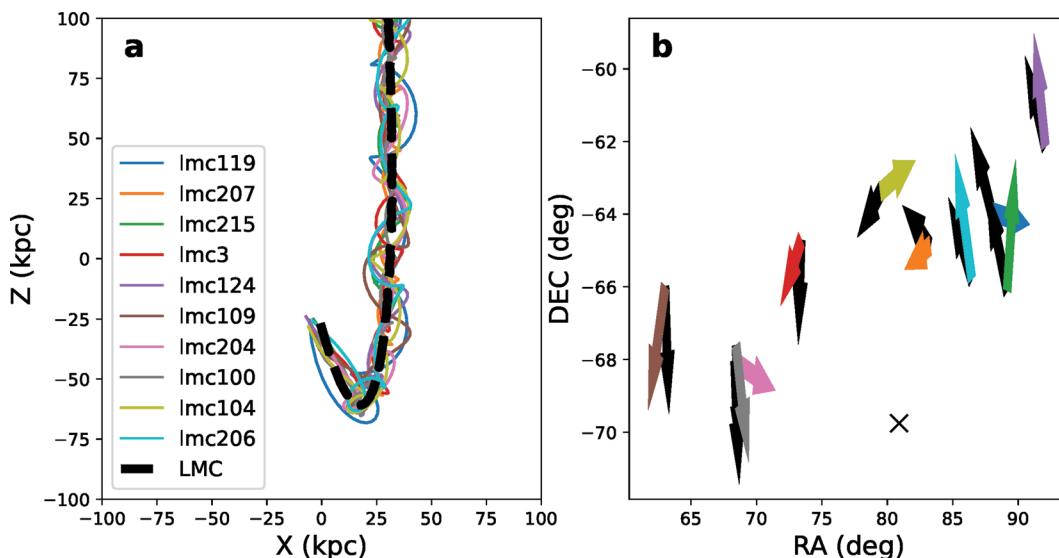
Peer review information *Nature Astronomy* thanks the anonymous reviewer(s) for their contribution to the peer review of this work.

Reprints and permissions information is available at
www.nature.com/reprints.

Publisher's note Springer Nature remains neutral with regard to jurisdictional claims in published maps and institutional affiliations.

Springer Nature or its licensor (e.g. a society or other partner) holds exclusive rights to this article under a publishing agreement with the author(s) or other rightholder(s); author self-archiving of the accepted manuscript version of this article is solely governed by the terms of such publishing agreement and applicable law.

© The Author(s), under exclusive licence to Springer Nature Limited 2024



Extended Data Fig. 1 | Orbit and proper motion analyses of metal-poor LMC stars in this study. **a.** The orbit of the LMC and stars observed in this study in Galactocentric X and Z coordinates, when integrated backwards in a potential that includes the Milky Way and the LMC²⁰. The LMC is shown as a thick dashed line, and stars in Table 1 are overplotted. Note that the stars remain bound to the LMC, indicating that they are gravitationally bound members. **b.** Proper motion vectors with respect to the center of mass motion of the LMC. The proper

motions of the stars observed in our study are shown as colored arrows, with the color scheme corresponding to panel (a). The black arrows indicate the average proper motion vector of LMC stars within 0.5° of their spatial location. Note that two of the LMC low metallicity stars are counter-rotating on the plane of the sky with respect to the bulk motion of LMC members, in the center-of-mass frame of the LMC. The center of the LMC is marked by a black cross.

Extended Data Table 1 | Summary of our observations of stars in the Large Magellanic Cloud

Name	RA	DEC	g	t_{exp} (min)	Date	Instrument
LMC-003	04:53:37.090	-64:43:57.55	17.05	100	30 Nov, 2022	MIKE
LMC-100	04:33:47.361	-67:37:31.51	17.36	25	1 Dec, 2022	MIKE
				80	19 Dec, 2022	MIKE
LMC-104	05:18:01.352	-63:22:26.56	16.50	15	1 Dec, 2022	MIKE
				30	19 Dec, 2022	MIKE
				30	20 Dec, 2022	MIKE
LMC-109	04:12:01.964	-66:00:58.36	17.01	20	19 Dec, 2022	MIKE
				40	20 Dec, 2022	MIKE
LMC-119	05:51:51.026	-63:56:37.60	16.85	105	1 Dec, 2022	MIKE
LMC-124	06:08:14.982	-62:07:23.33	16.76	60	20 Dec, 2022	MIKE
LMC-204	04:33:20.143	-68:02:41.87	17.30	47	1 Dec, 2022	MIKE
LMC-206	05:45:46.652	-65:46:35.40	17.08	110	1 Dec, 2022	MIKE
LMC-207	05:32:54.917	-64:53:09.88	17.10	115	1 Dec, 2022	MIKE
LMC-215	05:56:37.323	-66:05:17.85	17.16	105	19 Dec, 2022	MIKE
LMC-319	05:38:55.896	-64:21:50.52	17.33	15	17 Mar, 2023	MagE
LMC-323	06:17:10.604	-73:59:35.81	17.46	10	16 Mar, 2023	MagE
LMC-400	05:08:33.774	-72:25:27.55	16.82	15	27 Jan, 2023	MIKE
LMC-402	04:28:27.512	-69:22:08.36	17.21	20	27 Jan, 2023	MIKE
LMC-403	05:27:13.519	-65:11:46.17	17.06	15	27 Jan, 2023	MIKE
LMC-404	04:35:40.896	-66:09:29.18	17.45	15	17 Mar, 2023	MagE
LMC-405	04:54:16.665	-64:50:01.06	17.38	25	27 Jan, 2023	MIKE
LMC-406	05:15:58.050	-64:49:18.10	16.87	12.5	27 Jan, 2023	MIKE
LMC-407	04:55:47.448	-64:12:45.29	17.33	20	27 Jan, 2023	MIKE
LMC-409	05:55:03.971	-63:54:43.19	16.95	15	27 Jan, 2023	MIKE
LMC-410	05:42:10.807	-63:53:20.39	17.26	20	27 Jan, 2023	MIKE
LMC-411	05:29:44.001	-63:54:12.14	16.69	12.5	27 Jan, 2023	MIKE
LMC-413	05:37:05.212	-64:34:42.64	16.86	12.5	27 Jan, 2023	MIKE
LMC-414	05:27:13.879	-61:48:50.35	17.16	20	27 Jan, 2023	MIKE
LMC-416	06:45:46.181	-66:29:56.95	16.84	12.5	27 Jan, 2023	MIKE
LMC-007	05:44:58.823	-72:41:45.25	17.04	20	30 Nov, 2022	MIKE
LMC-008	06:27:25.744	-67:01:18.05	16.90	20	30 Nov, 2022	MIKE
LMC-101	04:42:26.547	-65:45:50.31	17.07	20	30 Nov, 2022	MIKE
LMC-116	05:46:35.167	-64:20:32.05	17.18	15	30 Nov, 2022	MIKE
LMC-202	05:04:52.769	-72:20:42.85	17.42	25	19 Dec, 2022	MIKE
LMC-217	05:44:00.168	-62:10:47.41	17.08	25	19 Dec, 2022	MIKE

The Right Ascension (RA) and Declination (DEC) columns indicate the position of the star in the sky. g is the SkyMapper magnitude as inferred from the Gaia XP spectra. t_{exp} is the total exposure time in minutes, with exposures on separate dates separated by a semicolon. The dates list the night of observation, with multiple nights of observation separated by a semicolon. The last column lists the instrument used for the observation.

Extended Data Table 2 | Properties of low metallicity LMC stars observed for short-durations on MIKE and MagE to solely derive metallicities and carbon abundances

Name	Teff (K)	Log(g)	v_mic (km/s)	[Fe/H]	[C/Fe]	[C/Fe]_c
LMC-319	4631±150	1.29±0.30	2.05±0.2	-2.69±0.24	-0.20±0.36	0.41±0.36
LMC-323	4609±150	1.25±0.30	2.08±0.2	-2.10±0.32	-0.80±0.47	-0.18±0.47
LMC-400	4422±150	0.9±0.30	2.26±0.2	-2.85±0.28	-0.42±0.27	0.31±0.27
LMC-402	4545±150	1.12±0.30	2.14±0.2	-3.20±0.25	<-0.10	<0.64
LMC-403	4504±150	1.05±0.30	2.18±0.2	-2.55±0.36	-0.49±0.28	0.26±0.28
LMC-404	4676±150	1.38±0.30	2.01±0.2	-2.42±0.32	-0.55±0.34	0.03±0.34
LMC-405	4653±150	1.33±0.30	2.04±0.2	-2.50±0.31	-0.35±0.28	0.26±0.28
LMC-406	4463±150	0.97±0.30	2.22±0.2	-2.22±0.41	-0.54±0.28	0.19±0.28
LMC-407	4631±150	1.29±0.30	2.05±0.2	-2.01±0.42	-0.49±0.28	0.09±0.28
LMC-409	4504±150	1.04±0.30	2.18±0.2	-2.63±0.21	<-0.55	<0.21
LMC-410	4609±150	1.25±0.30	2.07±0.2	-2.64±0.36	-0.41±0.27	0.21±0.27
LMC-411	4382±150	0.83±0.30	2.3±0.2	-2.79±0.17	<-0.45	<0.28
LMC-413	4463±150	0.97±0.30	2.22±0.2	-2.37±0.44	-0.68±0.26	0.10±0.26
LMC-414	4587±150	1.2±0.30	2.1±0.2	-2.30±0.22	-0.37±0.28	0.31±0.28
LMC-416	4443±150	0.94±0.30	2.24±0.2	-2.48±0.22	-0.59±0.27	0.03±0.27

Derived parameters of low metallicity LMC stars observed for short durations in Extended Data Table 1. The name of the star is followed by its derived effective temperature in Kelvin (Teff), surface gravity (logg), and microturbulence in km/s (v_mic). The metallicity ([Fe/H]), carbon abundance derived from the spectrum ([C/Fe]), and carbon abundance corrected for the evolutionary state of the star ([C/Fe]_c) following ref. 31 are listed.

Terms and Conditions

Springer Nature journal content, brought to you courtesy of Springer Nature Customer Service Center GmbH (“Springer Nature”). Springer Nature supports a reasonable amount of sharing of research papers by authors, subscribers and authorised users (“Users”), for small-scale personal, non-commercial use provided that all copyright, trade and service marks and other proprietary notices are maintained. By accessing, sharing, receiving or otherwise using the Springer Nature journal content you agree to these terms of use (“Terms”). For these purposes, Springer Nature considers academic use (by researchers and students) to be non-commercial.

These Terms are supplementary and will apply in addition to any applicable website terms and conditions, a relevant site licence or a personal subscription. These Terms will prevail over any conflict or ambiguity with regards to the relevant terms, a site licence or a personal subscription (to the extent of the conflict or ambiguity only). For Creative Commons-licensed articles, the terms of the Creative Commons license used will apply.

We collect and use personal data to provide access to the Springer Nature journal content. We may also use these personal data internally within ResearchGate and Springer Nature and as agreed share it, in an anonymised way, for purposes of tracking, analysis and reporting. We will not otherwise disclose your personal data outside the ResearchGate or the Springer Nature group of companies unless we have your permission as detailed in the Privacy Policy.

While Users may use the Springer Nature journal content for small scale, personal non-commercial use, it is important to note that Users may not:

1. use such content for the purpose of providing other users with access on a regular or large scale basis or as a means to circumvent access control;
2. use such content where to do so would be considered a criminal or statutory offence in any jurisdiction, or gives rise to civil liability, or is otherwise unlawful;
3. falsely or misleadingly imply or suggest endorsement, approval , sponsorship, or association unless explicitly agreed to by Springer Nature in writing;
4. use bots or other automated methods to access the content or redirect messages
5. override any security feature or exclusionary protocol; or
6. share the content in order to create substitute for Springer Nature products or services or a systematic database of Springer Nature journal content.

In line with the restriction against commercial use, Springer Nature does not permit the creation of a product or service that creates revenue, royalties, rent or income from our content or its inclusion as part of a paid for service or for other commercial gain. Springer Nature journal content cannot be used for inter-library loans and librarians may not upload Springer Nature journal content on a large scale into their, or any other, institutional repository.

These terms of use are reviewed regularly and may be amended at any time. Springer Nature is not obligated to publish any information or content on this website and may remove it or features or functionality at our sole discretion, at any time with or without notice. Springer Nature may revoke this licence to you at any time and remove access to any copies of the Springer Nature journal content which have been saved.

To the fullest extent permitted by law, Springer Nature makes no warranties, representations or guarantees to Users, either express or implied with respect to the Springer nature journal content and all parties disclaim and waive any implied warranties or warranties imposed by law, including merchantability or fitness for any particular purpose.

Please note that these rights do not automatically extend to content, data or other material published by Springer Nature that may be licensed from third parties.

If you would like to use or distribute our Springer Nature journal content to a wider audience or on a regular basis or in any other manner not expressly permitted by these Terms, please contact Springer Nature at

onlineservice@springernature.com